Check for updates

Received: 14 April 2022 | Revised: 14 June 2022 | Accepted: 3 August 2022

DOI: 10.1002/jcc.26997

RESEARCH ARTICLE

Journal of COMPUTATIONAL CHEMISTRY WILEY

Toward more potent imidazopyridine inhibitors of *Candida albicans* Bdf1: Modeling the role of structural waters in selective ligand binding

Yingsheng Zhou[1] | Justin M. Overhulse[1] | Nathan J. Dupper[1] | Yanchun Guo[1] | Boris A. Kashemirov[1] | Kaiyao Wei[2,3] | Jérôme Govin[3] | Carlo Petosa[2] | Charles E. McKenna[1]

[1]Department of Chemistry, University of Southern California, Los Angeles, California, USA

[2]Univ. Grenoble Alpes, CEA, CNRS, Institut de Biologie Structurale (IBS), Grenoble, 38000, France

[3]Univ. Grenoble Alpes, Inserm, CNRS, Institute for Advanced Biosciences (IAB), Grenoble, 38000, France

Correspondence
Charles E. McKenna, Department of Chemistry, University of Southern California, Los Angeles, CA 90089, USA.
Email: mckenna@usc.edu

Funding information
ANR, Grant/Award Number: ANR-18-CE18-0007; CEA PhD fellowship; Fondation Innovations en Infectiologie; National Institutes of Health, Grant/Award Numbers: R21 AI113704, T32 GM118289; USC Bridge Institute; Finovi Foundation

Abstract

Novel agents to treat invasive fungal infections are urgently needed because the small number of established targets in pathogenic fungi makes the existing drug repertoire particularly vulnerable to the emergence of resistant strains. Recently, we reported that *Candida albicans* Bdf1, a bromodomain and extra-terminal domain (BET) bromodomain with paired acetyl-lysine (AcK) binding sites (BD1 and BD2) is essential for fungal cell growth and that an imidazopyridine (**1**) binds to BD2 with selectivity versus both BD1 and human BET bromodomains. Bromodomain binding pockets contain a conserved array of structural waters. Molecular dynamics simulations now reveal that one water molecule is less tightly bound to BD2 than to BD1, explaining the site selectivity of **1**. This insight is useful in the performance of ligand docking studies to guide design of more effective Bdf1 inhibitors, as illustrated by the design of 10 new imidazopyridine BD2 ligands **1a–j**, for which experimental binding and site selectivity data are presented.

KEYWORDS
antifungal drugs, bromodomains, BET inhibition, *Candida albicans*, molecular dynamics, receptor-binding model, structural water

1 | INTRODUCTION

Invasive fungal infections (IFIs) have a high morbidity and mortality rate (overall 3-month mortality rate of 51% in one US study)[1] in immunocompromised lupus erythematosus, solid organ transplant or AIDS patients, and are estimated to cause more than 1.5 million deaths annually.[2] These systemic fungal infections are becoming more common, and often lack effective drug therapies.[3,4] *Candida* bloodstream infections are among the most significant IFIs among hospitalized patients, with a 30-day mortality rate of 41% according to a study conducted in Scotland in 2012–2013.[5] *Candida albicans* is the most common cause of *Candida* bloodstream infections, while *Candida glabrata* ranks second in isolation frequency.[6] *Candida auris*, a new multidrug-resistant species that causes nosocomial transmission has been identified as an emerging urgent global health threat by the Centers for Disease Control and Prevention (CDC).[7] Legacy antifungal strategies target cell membrane integrity (polyene drugs, e.g., amphotericin B), the synthesis of ergosterol (azole drugs such as fluconazole),[8] nucleic acid polymerases (pyrimidine analogues like

This is an open access article under the terms of the Creative Commons Attribution-NonCommercial-NoDerivs License, which permits use and distribution in any medium, provided the original work is properly cited, the use is non-commercial and no modifications or adaptations are made.
© 2022 The Authors. *Journal of Computational Chemistry* published by Wiley Periodicals LLC.

flucytosine)[9] or the cell wall (echinocandins)[10] with newer inhibitors targeting fungal dihydroorotate dehydrogenase (olorofim) and a Gwt1 (fosmanogepix).[3] However, the relatively limited number of drug classes available coupled with the increasing frequency of drug-resistant fungal strains[11,12] have created an urgent need for new approaches to antifungal drug design.[3,4,13]

Targeting of chromatin signaling pathways via small-molecule inhibition of bromodomain and extra-terminal domain (BET) bromodomains has been introduced as a therapeutic strategy against cancer and other non-infectious diseases[14,15] but had not been explored as an approach to antifungal drug discovery prior to our initial report on the structure, function and inhibition of *C. albicans* BET bromodomains.[16]

BET proteins are chromatin-associated factors that regulate gene transcription and chromatin organization.[17] BET proteins contain two bromodomains (BD1 and BD2), small helical domains that specifically recognize short peptides acetylated on lysine residues and that mediate the association of BET proteins with acetylated histones in chromatin.[15] Whereas humans have four BET proteins (Brdt, Brd2, Brd3, and Brd4), only a single BET protein (Bdf1) is present in *C. albicans*. We previously showed that mutations inactivating the ligand binding functionality of both Bdf1 bromodomains suppress the viability and virulence of *C. albicans*.[16] Using a homogeneous time-resolved FRET (HTRF) acetylpeptide ligand binding assay for Bdf1 bromodomains, we carried out a high-throughput chemical screen to identify Bdf1 bromodomain inhibitors. One promising hit identified was an imidazopyridine compound (compound **1**). This compound inhibited Bdf1 BD2 with a low micromolar IC_{50} value and showed selectivity against the orthologous BD2 domain from the human BET protein Brd4.[16]

Many successful drugs have emerged from high-throughput screen augmented by computer-aided rational design in recent years.[18–21] Computer-aided rational design can greatly accelerate the hit-to-lead phase of drug development and reduce the associated costs.[18] Despite recent advances in both computational capabilities[22,23] and efficient screening strategies,[24] drug discovery can still be complicated by complexities in ligand/binding site interactions. In this study of computer modeling-based Bdf1 bromodomain inhibitor optimization, we apply ligand binding site docking and molecular dynamics (MD) to analyze the ligand binding pocket interactions of *C. albicans* Bdf1 BD2 (hereafter *Ca*BD2), including the role of structural waters, with a series of designed analogues of **1**.

2 | METHODS

2.1 | Chemistry

All reagents and solvents were purchased from Sigma Aldrich, TCI or Oakwood Chemical and were used directly as received. Reaction products were purified by flash chromatography using the ISCO CombiFlash® Rf+ Lumen. ^{1}H, ^{13}C, and ^{19}F NMR spectra were obtained on Varian 400-MR, VNMRS-500, or VNMRS-600 spectrometers. NMR spectra were processed with MestReNova 9.0.0 or 11.0.2. Multiplicities are quoted as singlet (s), doublet (d), triplet (t), unresolved multiplet (m), doublet of doublets (dd), doublet of doublet of doublets (ddd), doublet of triplets (dt), triplet of doublets (td), and broad (b). All chemical shifts (δ) are reported in parts per million (ppm) relative to residual CD_2HOD in CD_3OD (δ 3.34, ^{1}H NMR), $CHCl_3$ in $CDCl_3$ (δ 7.26, ^{1}H NMR) and $CFCl_3$ (δ 0.00, ^{19}F NMR). Mass spectrometry was performed on a Finnigan LCQ Deca XP Max. Mass spectral data were calculated using ChemDraw 19.1.21. Isotopic mass for compounds containing a bromine atom was calculated for ^{81}Br. Compound IUPAC names were assigned by MarvinSketch 20.3.

2.2 | General method for synthesis of 1a–j

The **1a–j** series was prepared via a two-step reaction (Scheme 1) as previously reported.[16] The bromoacetophenone **3** (1 eq) and corresponding toluidine **4** (1.1 eq) were triturated with Na_2CO_3 (0.47 eq) for 2 min to form the α-aminoketone intermediates **5** (TLC). The product was washed 3× with water and dried under vacuum, then was dissolved in aqueous *i*PrOH (0.16 M). 3-Methylpyridin-2-amine (1 eq) was added dropwise, followed by ZnI_2 (0.3 eq), and 4 Å molecular sieves. The reaction mixture was heated to 80°C for 12 h, and the product **1** was taken up into EtOAc and purified via flash chromatography (Hex/EtOAc, 0%–90% gradient) (5%–20%).

2-Fluoro-4-(8-methyl-3-(p-tolylamino)imidazo[1,2-a]pyridin-2-yl) phenol (**1a**). ^{1}H NMR (400 MHz, CD_3OD): δ 7.80 (dq, J = 6.8, 0.8 Hz, 1H), 7.68 (dd, J = 12.8, 2.0 Hz, 1H), 7.61 (ddd, J = 8.4, 2.1, 1.0 Hz, 1H), 7.12 (dt, J = 6.8, 1.1 Hz, 1H), 6.98–6.92 (m, 2H), 6.90 (dd, J = 9.1, 8.4 Hz, 1H), 6.79 (t, J = 6.8 Hz, 1H), 6.44–6.40 (m, 2H), 2.62 (s, 3H), 2.20 (s, 3H); ^{13}C NMR (101 MHz, CD_3OD): δ 152.58, 150.20, 144.61, 144.47, 143.12, 142.54, 129.64, 127.96, 126.34, 124.48, 123.29 (d, J = 3.2 Hz), 120.69, 117.19 (d, J = 3.3 Hz), 114.60, 114.40, 112.84, 112.17, 19.09, 15.27; ^{19}F NMR (376 MHz, CD_3OD): δ 139.62 (dd, J = 12.9, 9.3 Hz); LRMS (ESI, m/z): $[M+H]^+$ calcd for $C_{21}H_{19}FN_3O$, 348.15; found, 348.60 (Figures S3–S7).

3-Fluoro-4-(8-methyl-3-(p-tolylamino)imidazo[1,2-a]pyridin-2-yl) phenol (**1b**). ^{1}H NMR (400 MHz, CD_3OD, δ): 7.79 (dq, J = 6.7, 0.7 Hz, 1H), 7.42 (t, J = 8.5 Hz, 1H), 7.15 (dt, J = 6.8, 1.2 Hz, 1H), 6.94–6.88 (m, 2H), 6.83 (t, J = 6.8 Hz, 1H), 6.63 (dd, J = 8.5, 2.4 Hz, 1H), 6.56 (dd, J = 12.0, 2.4 Hz, 1H), 6.39–6.32 (m, 2H), 2.61 (s, 3H), 2.18 (s, 3H); ^{13}C NMR (101 MHz, CD_3OD, δ): 163.40, 160.93, 160.41, 160.30, 144.44, 143.57, 132.85 (d, J = 5.4 Hz), 130.53, 128.88, 127.56, 125.38, 122.12, 114.23, 113.31, 112.17 (d, J = 3.0 Hz), 103.77, 103.52, 20.28, 16.49; ^{19}F NMR (376 MHz, CD_3OD): −114.06 (dd, J = 12.0, 8.5 Hz); LRMS (ESI, m/z): $[M+H]^+$ calcd for $C_{21}H_{19}FN_3O$, 348.15; found, 348.50 (Figures S8–S12).

5-((2-(4-Hydroxyphenyl)-8-methylimidazo[1,2-a]pyridin-3-yl)amino)-2-methylphenol (**1c**). ^{1}H NMR (600 MHz, CD_3OD): δ 7.82–7.80 (m, 2H), 7.80 (d, J = 2.1 Hz, 1H), 7.11 (dt, J = 6.9, 1.2 Hz, 1H), 6.85 (d, J = 8.1 Hz, 1H), 6.80 (dd, J = 4.4, 2.4 Hz, 2H), 6.79 (d, J = 1.9 Hz, 1H), 6.07 (dd, J = 8.1, 2.3 Hz, 1H), 5.91 (d, J = 2.3 Hz, 1H), 2.61 (s, 3H), 2.06 (s, 3H); LRMS (ESI, m/z): $[M+H]^+$ calcd for $C_{21}H_{20}N_3O_2$, 346.16 m/z; found, 346.30 (Figures S13–S15).

1096987x, 2022, 32, Downloaded from https://onlinelibrary.wiley.com/doi/10.1002/jcc.26997 by Cea Grenoble, Wiley Online Library on [24/07/2024]. See the Terms and Conditions (https://onlinelibrary.wiley.com/terms-and-conditions) on Wiley Online Library for rules of use; OA articles are governed by the applicable Creative Commons License

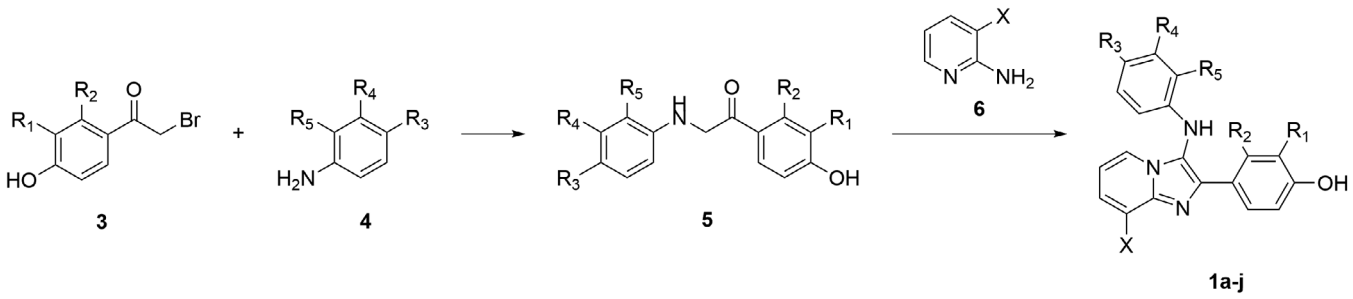

SCHEME 1 Synthesis of **1a–j**.

2-((2-(4-Hydroxyphenyl)-8-methylimidazo[1,2-a]pyridin-3-yl)amino)-5-methylphenol (**1d**). ^{1}H NMR (400 MHz, CD_3OD): δ 7.85–7.78 (m, 3H), 7.11 (dt, J = 6.8, 1.2 Hz, 1H), 6.82–6.75 (m, 3H), 6.68 (dd, J = 1.8, 0.7 Hz, 1H), 6.38–6.30 (m, 1H), 5.86 (d, J = 7.9 Hz, 1H), 2.62 (s, 3H), 2.16 (s, 3H); ^{13}C NMR (101 MHz, CD_3OD): δ 157.02, 144.52, 142.42, 138.40, 131.23, 128.41, 128.35, 126.05, 124.67, 124.25, 120.70, 120.04, 115.16, 114.75, 111.95, 111.52, 19.33, 15.28; LRMS (ESI, m/z): $[M+H]^+$ calcd for $C_{21}H_{20}N_3O_2$, 346.16; found, 346.40 (Figures S16–S19).

4-(8-Chloro-3-(p-tolylamino)imidazo[1,2-a]pyridin-2-yl)phenol (**1e**). ^{1}H NMR (400 MHz, CD_3OD, δ): 7.89 (dt, J = 6.8, 1.0 Hz, 1H), 7.88–7.75 (m, 2H), 7.39 (dd, J = 7.4, 1.0 Hz, 1H), 7.02–6.89 (m, 2H), 6.89–6.71 (m, 3H), 6.48–6.36 (m, 2H), 2.20 (s, 3H); LRMS (ESI, m/z): $[M+H]^+$ calcd for $C_{20}H_{17}ClN_3O$, 350.11; found, 350.36 (Figures S20–S22).

4-(8-Bromo-3-(p-tolylamino)imidazo[1,2-a]pyridin-2-yl)phenol (**1f**). ^{1}H NMR (600 MHz, CD_3OD) δ: 7.94 (dd, J = 6.7, 1.0 Hz, 1H), 7.85–7.79 (m, 2H), 7.58 (dd, J = 7.3, 1.0 Hz, 1H), 6.98–6.94 (m, 2H), 6.80–6.76 (m, 3H), 6.44–6.39 (m, 2H), 2.20 (s, 3H); ^{13}C NMR (151 MHz, CD_3OD: δ 158.80, 144.32, 141.31, 141.25, 131.10, 130.05, 129.53, 129.05, 125.54, 123.76, 121.72, 116.23, 114.33, 113.44, 111.46, 20.51); LRMS (ESI, m/z): $[M+H]^+$ calcd for $C_{20}H_{17}BrN_3O$, 396.05; found, 396.35 (Figures S23–S26).

4-(8-Iodo-3-(p-tolylamino)imidazo[1,2-a]pyridin-2-yl)phenol (**1g**). ^{1}H NMR (600 MHz, CD_3OD): δ 7.93 (dd, J = 6.7, 1.1 Hz, 1H), 7.84–7.81 (m, 2H), 7.79 (dd, J = 7.1, 1.1 Hz, 1H), 6.98–6.94 (m, 2H), 6.80–6.75 (m, 2H), 6.63 (t, J = 6.9 Hz, 1H), 6.45–6.37 (m, 2H), 2.20 (s, 3H); ^{13}C NMR (151 MHz, CD_3OD): δ 157.29, 142.94, 141.51, 139.80, 134.51, 129.65, 128.61, 128.02, 124.24, 123.00, 120.30, 114.76, 112.88, 112.57, 82.56, 19.08; LRMS (ESI, m/z): $[M+H]^+$ calcd for $C_{20}H_{17}IN_3O$, 442.04; found, 442.22 (Figures S27–S30).

4-(3-([4-Aminophenyl]amino)-8-methylimidazo[1,2-a]pyridin-2-yl) phenol (**1h**). ^{1}H NMR (400 MHz, CD_3OD): δ 7.83–7.77 (m, 3H), 7.09 (dt, J = 6.9, 1.2 Hz, 1H), 6.80–6.75 (m, 3H), 6.64 (d, J = 8.6 Hz, 2H), 6.36 (d, J = 8.6 Hz, 2H), 2.61 (s, 3H); LRMS (ESI, m/z): $[M+H]^+$ calcd for $C_{20}H_{19}N_4O$, 331.16; found, 331.37 (Figures S31–S33).

4-(3-([4-Bromophenyl]amino)-8-methylimidazo[1,2-a]pyridin-2-yl) phenol (**1i**). ^{1}H NMR (600 MHz, CD_3OD): δ 7.80 (dd, J = 6.8, 1.0 Hz, 1H), 7.79–7.75 (m, 2H), 7.26–7.23 (m, 2H), 7.13 (dt, J = 6.9, 1.4 Hz, 1H), 6.83 (d, J = 6.8 Hz, 1H), 6.81–6.79 (m, 2H), 6.48–6.42 (m, 2H), 2.62 (s, 3H); ^{13}C NMR (151 MHz, CD_3OD): δ 157.21, 145.14, 142.63, 138.65, 131.91, 128.45, 126.34, 124.44, 124.38, 120.45, 118.01, 114.84, 114.60, 112.27, 110.13, 15.28; LRMS (ESI, m/z): $[M+H]^+$ calcd for $C_{20}H_{17}BrN_3O_3$, 396.05; found, 396.20 (Figures S34–S37).

4-(8-Methyl-3-([4-nitrophenyl]amino)imidazo[1,2-a]pyridin-2-yl)phenol (**1j**). ^{1}H NMR (400 MHz, CD_3OD): δ 8.14–8.03 (m, 2H), 7.85 (ddd, J = 6.8, 1.3, 0.7 Hz, 1H), 7.78–7.70 (m, 2H), 7.20 (d, J = 6.9 Hz, 0H), 6.88 (t, J = 6.8 Hz, 1H), 6.85–6.78 (m, 2H), 6.63 (d, J = 8.7 Hz, 2H), 2.65 (s, 3H); ^{13}C NMR (151 MHz, CD_3OD): δ 171.57, 157.44, 152.14, 142.97, 139.71, 139.03, 128.44, 126.60, 125.84, 124.70, 124.04, 120.28, 116.32, 114.94, 112.64, 15.29; LRMS (ESI, m/z): $[M+H]^+$ calcd for $C_{20}H_{17}N_4O_3$, 361.13; found, 361.43 (Figures S38–S41).

2.3 | Computational studies

2.3.1 | Dscore calculation

All chains in the published PDB structures were extracted and analyzed with inclusion of the five conserved structural waters located inside the binding pocket.[17] Structural waters were manually added to chains lacking all five conserved waters from complete chains. The chains were prepared and minimized using the Schrödinger Suite (release 2017-3) protein preparation wizard to ensure consistency using the force field OPLS3e.[25] The minimized chains were then analyzed using Schrödinger Suite SiteMap, to obtain the druggability score (Dscore) with default parameters.[26]

2.3.2 | Molecular docking

The atomic coordinates of *Ca*BD2 including those of the structural water molecules (W0–W5) were taken from the structure of *Ca*BD2 bound to imidazopyridine **1** (PDB code: 5N18). Ligand molecules were simulated as flexible, while the protein structure remained fixed, except for induced fit docking. The pH was set to 7 and all relevant structures at this pH were examined. For each high scoring molecule, docking was first performed in ICM-Pro Molecular Modeling Software (Molsoft) version 3.9-2b, with default settings. The molecule was then re-docked to the protein using Schrödinger Suite SP-Glide docking, with default settings. Finally, docking was redone using the Schrödinger Suite Induced Fit module, with residues near the binding pocket set to flexible.

1096987x, 2022, 32, Downloaded from https://onlinelibrary.wiley.com/doi/10.1002/jcc.26997 by Cea Grenoble, Wiley Online Library on [24/07/2024]. See the Terms and Conditions (https://onlinelibrary.wiley.com/terms-and-conditions) on Wiley Online Library for rules of use; OA articles are governed by the applicable Creative Commons License

2.3.3 | Molecular dynamics

The atomic coordinates of ligand-free *Ca*BD1 (PDB 5N15) and of the unbound (PDB 5N13) and **1**-bound (PDB 5N18) forms of *Ca*BD2 were prepared using the Schrödinger Suite protein preparation function at pH = 7. For each bromodomain, the conserved water molecules W0–W4 (as well as the non-conserved water W5) within the *Ca*BD2 binding pocket were kept, while all other water molecules were deleted. We replaced the glycerol molecule in the complexed *Ca*BD2 structure (PDB 5N15) by a water molecule, using the position of the corresponding W1 water molecule in unbound *Ca*BD1 as a reference. Then each protein with its bound water molecules was minimized using the protein preparation wizard. All the prepared proteins or protein-ligand systems were then uploaded to http://charmm-gui.org to generate the required GROMACS files, with Force Field CHARMM36m applied.[27] The water boxes were set to the default size, with Na^+ and Cl^- added to create 0.15 mM NaCl solution environments. The temperature was changed to 310 K and a 100 ns MD simulation was performed for each system using Gromacs 5.1.

2.3.4 | MD analysis

The trajectories were analyzed using the MD analysis tool WORDOM.[28,29] Occupancy of each conserved water molecule position was determined using the three atoms from the binding site residues list in Tables S1 and S2. The area of the intersection of three spheres was calculated using a Monte-Carlo method, with iteration set to 1e6.

2.4 | HTRF assay

The biotinylated tetra-acetylated histone H4 peptide ($H4Ac_4$, N-terminal H4 peptide, residues 1–20, with acetylation of K5, K8, K12 and K16) was purchased from Covalab (Villeurbanne, France). HTRF reagents and buffers were purchased from Cisbio. HTRF assays were performed as previously described.[16] Briefly, GST-tagged bromodomains (human Brd4 BD1 and BD2, *Ca*Bdf1 BD1 and BD2) in 25 mM Hepes pH 7.5, 150 mM NaCl, 0.5 mM DTT were assayed at 5 nM final concentration. The corresponding final concentrations of biotinylated $H4Ac_4$ peptide used were 50, 600, 300 and 400 nM, respectively. The antibody-conjugated donor (Mab anti-GST-Tb; Cisbio) was used at 0.5 nM and the streptavidin-conjugated acceptor (streptavidin-d2; Cisbio) was used at 1/8 of the $H4ac_4$ peptide concentration. Inhibitors were tested by performing a nine-point dilution series with a final concentration ranging between 0.013 and 20 μM. Experiments were performed in 384-well white plates (Greiner 781080) in a final volume of 16 μl. Plates were incubated at 4°C for 4 h (BD1) or 24 h (BD2) and subsequently analyzed in a ClarioStar plate reader (BMG LABTECH). Excitation was at 330 nm and emission intensities were measured at 620 and 665 nm with an integration delay of 60 μs and an integration time of 400 μs.

3 | RESULTS

3.1 | MD analysis of water molecules in the binding pocket of Bdf1 bromodomains

A highly conserved structural feature of bromodomains is an array of five water molecules (designated W0–W4) that form hydrogen bonds with protein main chain and side chain atoms within the ligand binding pocket,[15] as observed in the unliganded structure of *Ca*BD1 (Figure 1A). These water molecules, which reduce the volume and alter the shape of the binding pocket,[30] play an important role in ligand recognition since they can bridge hydrogen bonds between the ligand and protein residues.[31,32] They also affect the druggability of the pocket when present, as reflected in the change in Dscore (Figure S2 and Table S3; a higher Dscore corresponds to a more druggable pocket). Huang et al. have reported that some of these water molecules can be displaced by other solvents.[33] Interestingly, in the structure of unbound *Ca*BD2 (PDB 5N13), which was determined using crystals soaked in a glycerol-containing solution,[4] water position W1 is occupied by the hydroxyl group of a glycerol molecule (Figure 1B). Similarly, in the crystal structure of *Ca*BD2 bound to inhibitor **1** (PDB 5N18), position W1 is occupied by the hydroxyl group of the ligand (Figure 1C). In this structure, another (non-conserved) water molecule (W5) serves as a water bridge between the receptor and the ligand (Figure 1C).

We hypothesized that conserved water W1 in *Ca*BD2 is selectively displaced by ligands because it is relatively more weakly bound to the *Ca*BD2 ligand binding pocket. To verify this hypothesis, we applied the analysis method of Huang et al.[33] by monitoring the behavior of water molecules W0–W5 in MD simulations of *Ca*BD1 and *Ca*BD2 (Figure 2).

Three 100 ns MD analyses with identical parameters were separately conducted on *Ca*BD1 (PDB 5N15) and on the unbound (PDB 5N13) and **1**-bound (PDB 5N18) forms of *Ca*BD2 (Figure 3) (for unbound *Ca*BD2, the glycerol ligand was replaced by a water molecule at the W1 position). The position of each monitored water molecule was determined by three nearby protein atoms, with a preference for oxygen and nitrogen atoms that could form hydrogen bonds. Water occupancy was calculated using threshold values of distances between the water molecules and corresponding protein atoms (Tables S1 and S2). The threshold values were adjusted to keep a constant volume (22 ± 2 $Å^3$) at each water position.

The results reveal that the six water molecules in unbound *Ca*BD2 have very different occupancies (Figure 3). The position of water W1, which was displaced by the ligand in *Ca*BD2 (Figure 3C, 3D), had a relatively low water occupancy (~15%) compared to the other conserved water positions W0 and W2–W4 (~60%) (Figure 3B, 3D). In contrast, the W1 position in *Ca*BD1 had a high water occupancy (~80%), demonstrating that the presence of this water was energetically favorable (Figure 3A, 3D). Water W5, which is not a canonical conserved water in bromodomain structures, displayed a low water occupancy in *Ca*BD2 only (~15%) (Figure 3). In addition, comparing the water occupancies of the bound and unbound forms of

1096987x, 2022, 32, Downloaded from https://onlinelibrary.wiley.com/doi/10.1002/jcc.26997 by Cea Grenoble, Wiley Online Library on [24/07/2024]. See the Terms and Conditions (https://onlinelibrary.wiley.com/terms-and-conditions) on Wiley Online Library for rules of use; OA articles are governed by the applicable Creative Commons License

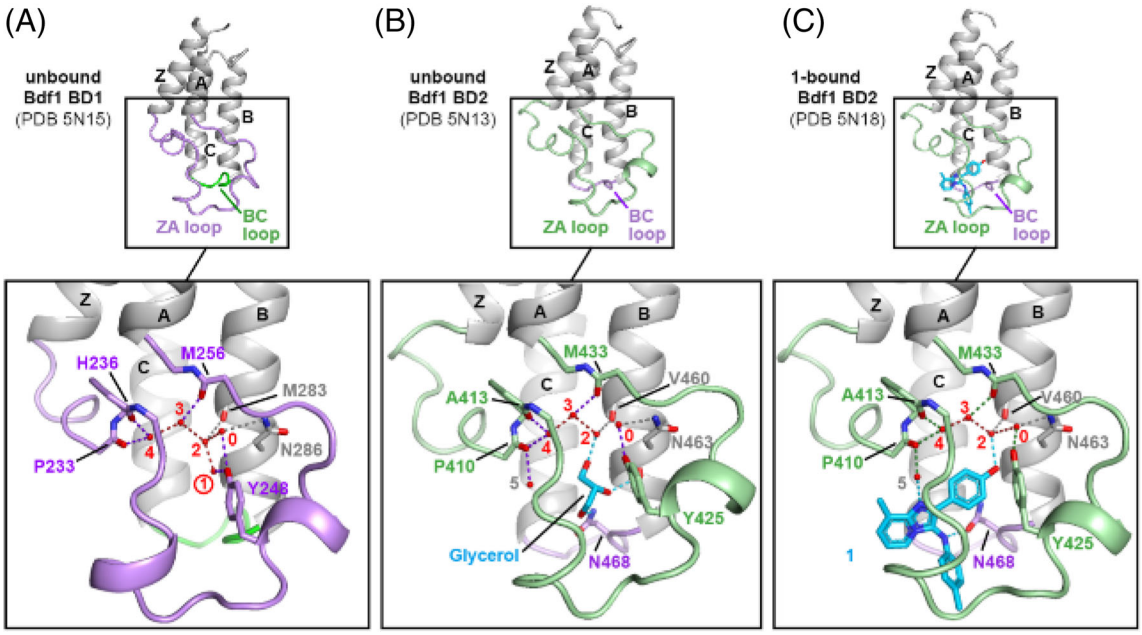

FIGURE 1 Comparison of the conserved water molecules (red number labels) of (A) *Ca*BD1 (PDB 5N15), (B) *Ca*BD2 (PDB 5N13) and (C) *Ca*BD2 bound to compound **1** (PDB 5N18)

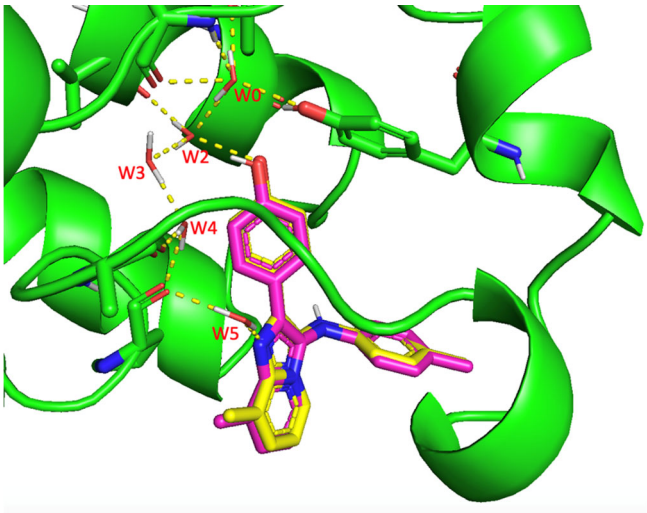

FIGURE 2 Overlap of the binding pose observed for **1** in the co-crystal structure with *Ca*BD2 (PDB 5N18) (yellow) with that predicted by molecular docking (pink)

*Ca*BD2 showed that the presence of the imidazopyridine ligand stabilized all five water molecules common to both forms (W0 and W2–W5), increasing the water occupancy by 5%–10% (Figure 3BD).

The difference in stability of water molecule W1 in *Ca*BD1 vs *Ca*BD2 contributes to the difference in water shell and pocket size between these two bromodomains. For ligand docking studies, it therefore is preferable to retain this W1 in the binding pocket of *Ca*BD1 and omit it in *Ca*BD2, although this presents a potential challenge in attempting to design single compounds that potently inhibit both BDs.

3.2 | Ligand docking studies

We next performed ligand docking studies using Schrödinger Suite SP-Glide docking to better understand how **1** interacts with the *Ca*BD2 binding pocket and aid identification of more effective ligands. First, we re-docked **1** to *Ca*BD2, retaining the conserved water molecules observed in the crystal structure (W0, W2–W5). The predicted binding pose with the non-protonated form of the ligand was essentially identical to that observed experimentally (Figure 2), enhancing confidence in the reliability of the docking procedure.

Because the occupancy of water W1 is significantly lower than that of the other conserved waters, we excluded it from the docking model. To confirm this choice and further validate the docking protocol, we docked the same ligand **1** to *Ca*BD2 with all six water molecules including W1. The resulting model gave a docking score of −7.25 kJ/mol, significantly worse than the score obtained when W1 was omitted (−9.90 kJ/mol). The interaction graph (Figure S1) now showed a poor fit for the ligand, which was forced partially outside the pocket by the additional water.

3.2.1 | The effect of pK_a on inhibitor potency

Our initial high-throughput chemical screen yielded a hit compound, **2**, that inhibited *Ca*BD2 much more potently than **1**. Using MarvinSketch 20.3 to estimate pK_a values for **2** and **1** (Figure 4), we found that the pK_a corresponding to the protonated imidazole nitrogen atom differed significantly between the two compounds: 3.10 in **2** versus 6.24 in **1**, owing to destabilization of the protonated species by the meta-pyridyl nitrogen (Figure S43).

1096987x, 2022, 32, Downloaded from https://onlinelibrary.wiley.com/doi/10.1002/jcc.26997 by Cea Grenoble, Wiley Online Library on [24/07/2024]. See the Terms and Conditions (https://onlinelibrary.wiley.com/terms-and-conditions) on Wiley Online Library for rules of use; OA articles are governed by the applicable Creative Commons License

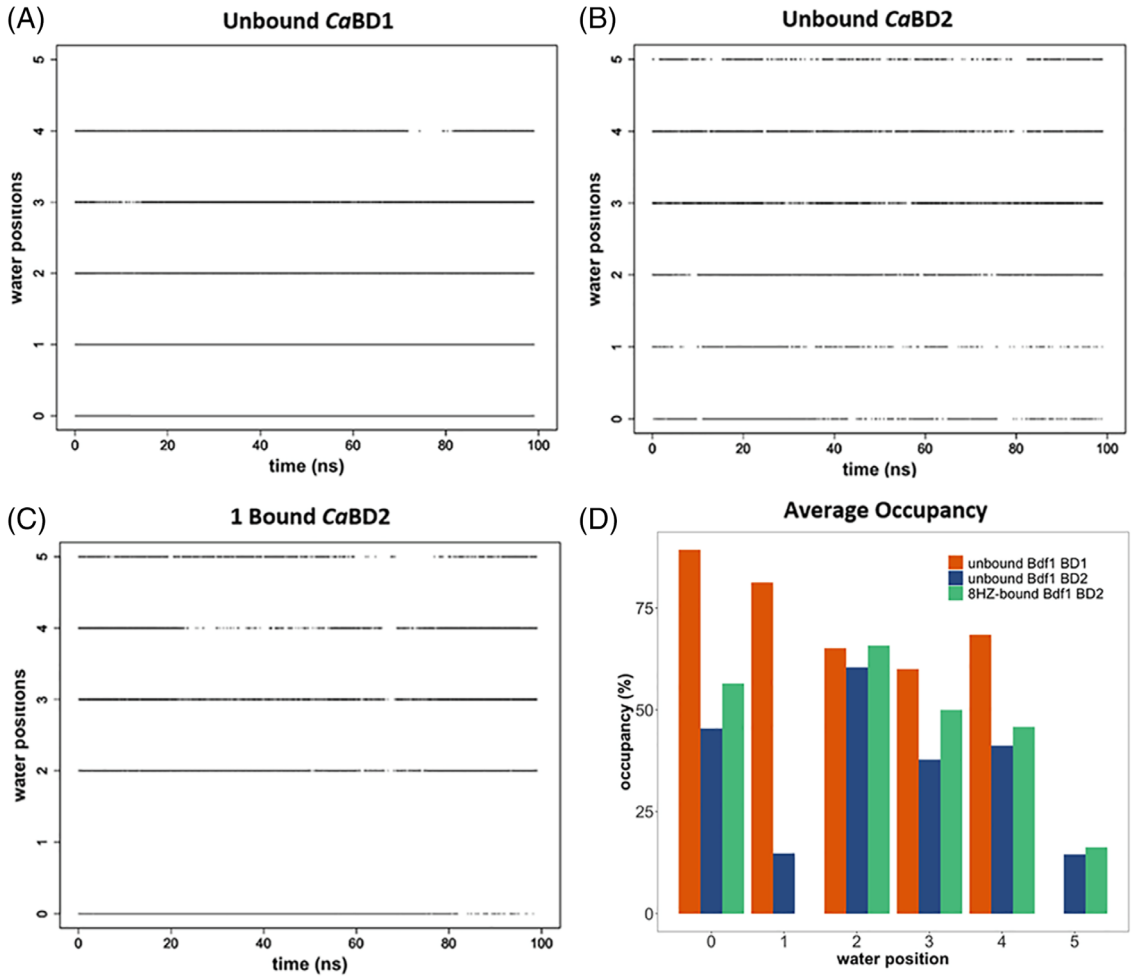

FIGURE 3 Occupancy of structural water positions in the binding pocket of *Ca*BD1 and BD2. (A–C) A data point indicates that a water molecule is present at a given time. (A) The dynamics of water molecules W0–W4 for unbound *Ca*BD1 (PDB 5N15). (B) The dynamics of water molecules W0–W5 for unbound *Ca*BD2 (PDB 5N13). (C) The dynamics of water molecules W0 and W2–W5 for 1-bound *Ca*BD2 (PDB 5N18; 8HZ = **1**). (D) Histogram comparing the water occupancy of positions W0–W5

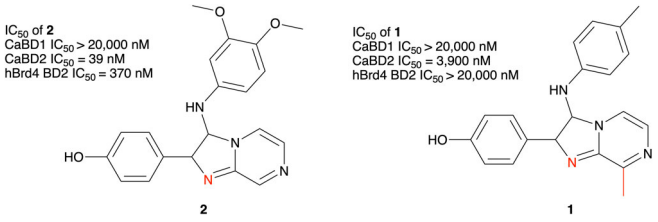

FIGURE 4 Structures of inhibitors **2** and **1**

To better understand the role of the ligand pK_a in binding, we docked **1** in both the non-protonated and protonated forms to *Ca*BD2 using Schrödinger Suite SP-GLIDE docking (Figure 5).

The modeling results revealed that non-protonated **1** had a score of −9.90 kJ/mol, while that of the protonated form was −8.86 kJ/mol. The ligand interaction diagram reveals that this difference may originate from a change in the bridging role of water molecule W5, which serves as a hydrogen donor instead of a hydrogen acceptor. The standard pK_a for all of the compounds are calculated to be within the range of 3.10–6.24 suggesting they would all be ionized at pH 7, promoting hydrogen bonding.

3.3 | Potential for additional polar interactions

The interaction diagram in Figure 5 shows that the methyl of the methylphenyl group of **1** is very close to leucine 420. The distance between the methyl group carbon of **1** and the backbone carbonyl oxygen of leucine 420 is 4.3 Å. One might be able to introduce additional polar interactions that enhance inhibitor potency by replacing the methyl group with a hydrogen donor or by adding hydrogen donor groups to the phenyl ring. Induced fit docking using the Schrödinger Suite supported this hypothesis. Adding a hydroxyl group in the ortho or meta position (**1c** and **1d**) with respect to the methyl group was predicted to yield an additional polar interaction with the Leu420 carbonyl group. Replacement of —CH_3 with —NH_2 did not show a notable improvement in the docking score (**1h**), but distance between the

1096987x, 2022, 32, Downloaded from https://onlinelibrary.wiley.com/doi/10.1002/jcc.26997 by Cea Grenoble, Wiley Online Library on [24/07/2024]. See the Terms and Conditions (https://onlinelibrary.wiley.com/terms-and-conditions) on Wiley Online Library for rules of use; OA articles are governed by the applicable Creative Commons License

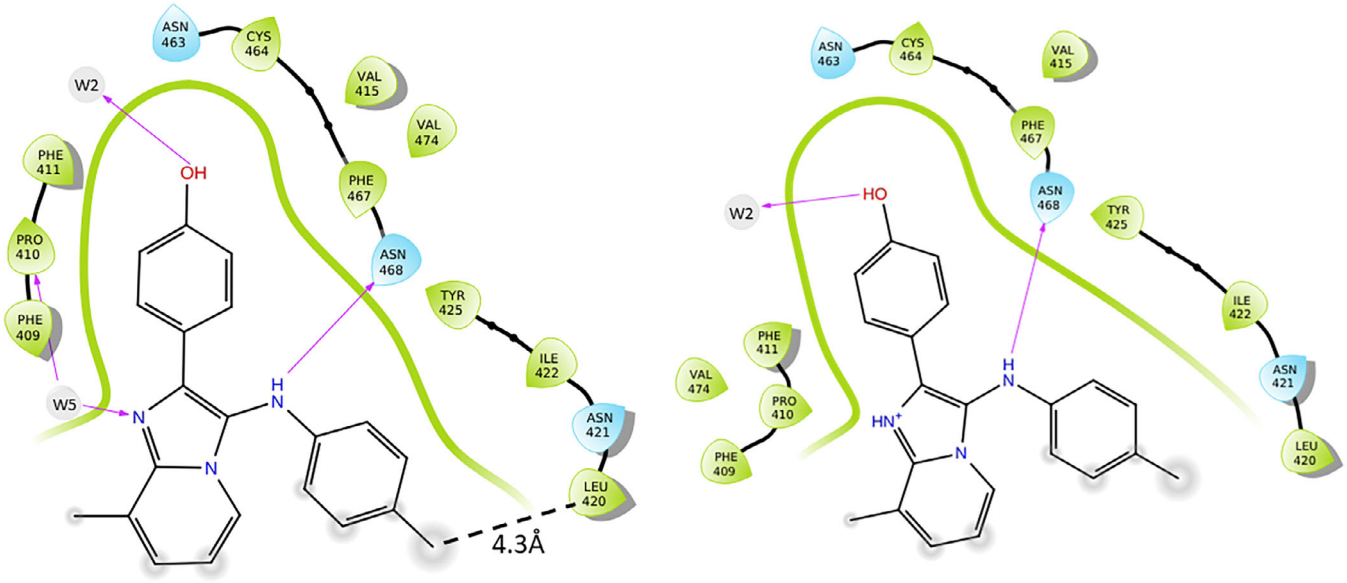

FIGURE 5 Binding interaction diagram of unprotonated (left) and protonated (right) **1** (PDB 5N18)

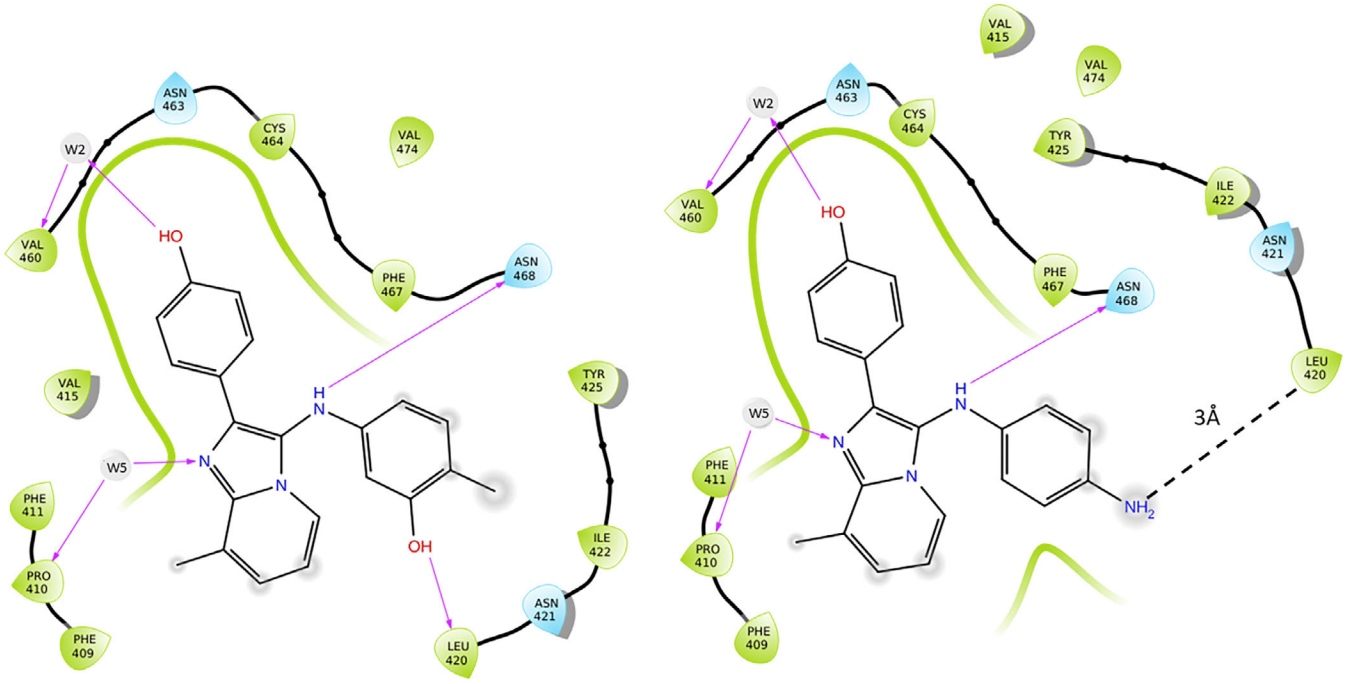

FIGURE 6 Binding mode of **1** analogues in induced fit docking (left: addition of —OH [**1c**]; right: replacement of —CH_3 with —NH_3 [**1h**])

—H from —NH_2 to the Leu420 oxygen is within 3 Å, suggesting the feasible formation of an additional hydrogen bond (Figure 6).

3.4 | Inhibitor design

As discussed above, when performing molecular docking we only retained the conserved waters observed in the ligand-bound *Ca*BD2 crystal structure (PDB 5N18). The docking was performed with ICM-Pro Molecular Modeling Software (Molsoft) version 3.9-2b using a total position scan. Analogues with relatively high docking score were selected and re-docked on *Ca*BD2 using Schrödinger Suite SP-Glide, via rigid and flexible pathways. The output compounds were then selected based on our analysis of the pocket property (Figure 7).

Compounds **1a–1b** were designed to enhance the hydrophobic interactions inside the pocket (residues F411, V415, Y425, C464, F467, V474), by introduction of an F substituent. In **1c–1d** and **1h**, we sought to enable additional hydrogen bonds with Leu420, as discussed above. Compounds **1e–1g** were designed to lower the

1096987x, 2022, 32, Downloaded from https://onlinelibrary.wiley.com/doi/10.1002/jcc.26997 by Cea Grenoble, Wiley Online Library on [24/07/2024]. See the Terms and Conditions (https://onlinelibrary.wiley.com/terms-and-conditions) on Wiley Online Library for rules of use; OA articles are governed by the applicable Creative Commons License

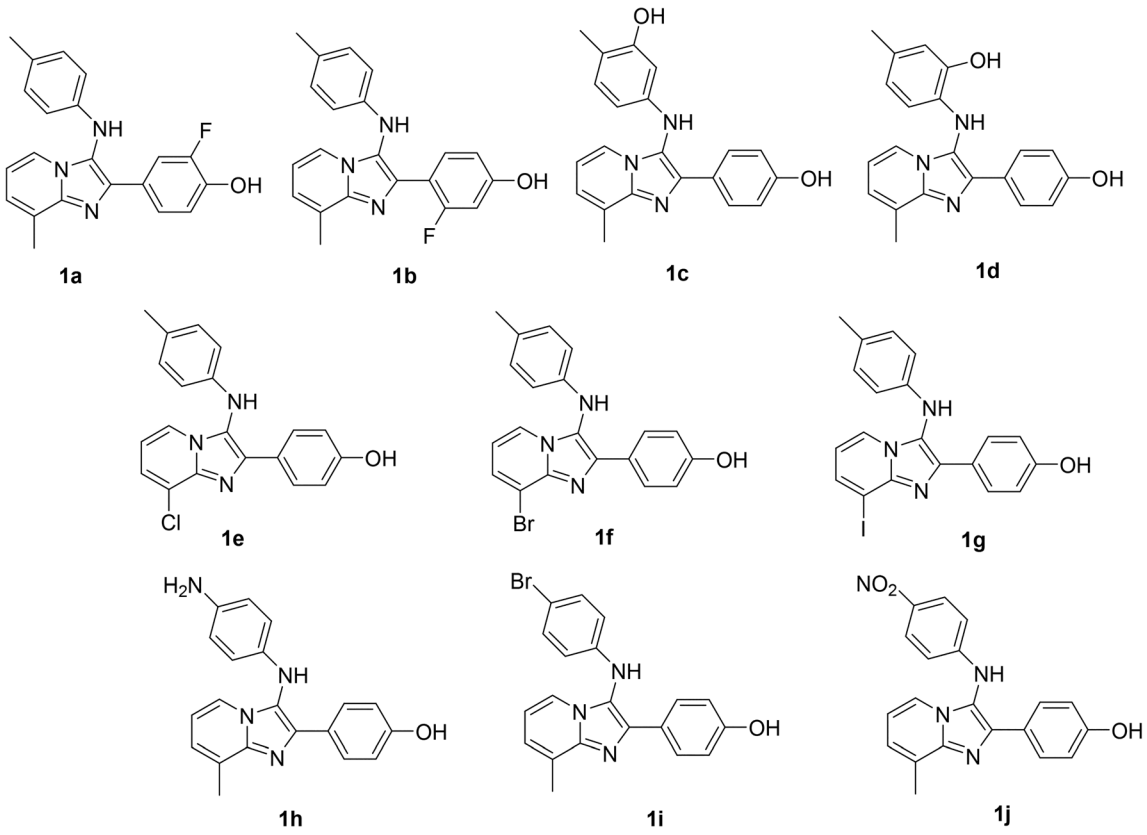

FIGURE 7 Designed analogues of **1**

pK_a of the target ligand by introducing electron-withdrawing substituents. The original imidazopyridine methyl group was replaced by halogen atoms (Cl, Br, or I) to mimic the electron density of compound **2** while preserving its selectivity. F was not considered in this role, because of its small size. In compounds **1i–1j** we replaced the toluidine methyl group with Br and NO_2 substituents, as prototypes for conjugation with a second drug.

3.5 | Synthesis

The **1a–1j** series of compounds were prepared via a two-step synthetic strategy (Scheme 1) originally developed for **1**.[16] Thus, the α-aminoketones **5** were formed by reaction of bromide **3** with toluidine **4**. Formation of the final imidazo[1,2-a]pyridines **1a–1j** was realized by Lewis acid-catalyzed condensation of the appropriate **5** derivative with 3-methylpyridin-2-amine (**6**) in the presence of oxygen. All compounds were characterized by their NMR and MS spectra.

3.6 | Inhibitory activity of compounds against *Ca*BD2

HTRF assays showed that compounds **1c**, **1e**, **1f**, **1g**, and **1h** have relatively higher potency (lower IC_{50} values) compared to **1**, consistent with the predictions made from molecular docking (Table 1, Figure S42). However, the addition of a fluorine atom in compounds **1a** and **1b** did not decrease the IC_{50} value. Compounds **1**c and **1**d with a hydroxyl group at R4 or R5, respectively, were not predicted to differ in potency, but in fact **1**c showed significantly increased potency compared to **1** and **1**d. The introduction of halogens in position X (**1e**, **1f**, and **1g**) showed no significant difference in potency between the three, as expected with the docking results, but compared to **1** increased potency. This is likely due to the decrease in pK_a of the nitrogen hydrogen bonding with W5 (Figure, Figure S43). **1h** showed increased hydrogen bonding with Leu420 based on docking results, and was shown to increase inhibition compared to **1**. When the methyl group in position R3 was replaced with a bromo or nitro group as in **1i** and **1j**, there was no significant decrease in activity as predicted by our docking results.

4 | DISCUSSION

Similarly to human BDs, *Ca*BDs contain a flexible binding pocket associated with structurally conserved waters that are necessary to take into account when performing computational modeling. A MD study of *Ca*BD1 and *Ca*BD2 reveals that the stability of the five conserved waters varies between binding sites. Structural water W1 in *Ca*BD2 was shown to be less stable than the other bound

1096987x, 2022, 32, Downloaded from https://onlinelibrary.wiley.com/doi/10.1002/jcc.26997 by Cea Grenoble, Wiley Online Library on [24/07/2024]. See the Terms and Conditions (https://onlinelibrary.wiley.com/terms-and-conditions) on Wiley Online Library for rules of use; OA articles are governed by the applicable Creative Commons License

TABLE 1 IC_{50} of ligand analogues **1a–j**

Comp	R_1	R_2	R_3	R_4	R_5	X	ICM-pro docking scores (CaBD2, unitless)	IC_{50} (μM)				Selectivity (CaBD2 vs. hBrd4 BD2)
								*Ca*BD1	CaBD2	hBrd4 BD1	hBrd4 BD2	
1							−42.04	>20	3.90 ± 0.35	>20	>20	>5
1a	—F	—H	—Me	—H	—H	—Me	−41.31	>20	6.30 ± 2.78	14.8 ± 6.9	8.7 ± 1.8	1.4
1b	—H	—F	—Me	—H	—H	—Me	−41.73	>20	5.22 ± 2.12	>20	>20	>4
1c	—H	—H	—Me	—OH	—H	—Me	−41.47	>20	0.78 ± 0.15	>20	>20	>26
1d	—H	—H	—Me	—H	—OH	—Me	−41.89	>20	9.74 ± 0.19	>20	>20	>2
1e	—H	—H	—Me	—H	—H	—Cl	−43.21	>20	1.50 ± 0.42	>20	16.0 ± 1.2	10.6
1f	—H	—H	—Me	—H	—H	—Br	−43.69	>20	0.75 ± 0.25	>20	>20	>26
1g	—H	—H	—Me	—H	—H	—I	−44.09	>20	1.01 ± 0.19	>20	>20	>20
1h	—H	—H	$—NH_2$	—H	—H	—Me	−41.20	>20	0.37 ± 0.09	>20	2.24 ± 0.65	6.1
1i	—H	—H	—Br	—H	—H	—Me	−41.68	>20	4.35 ± 0.63	>20	12.8 ± 3.2	2.9
1j	—H	—H	$—NO_2$	—H	—H	—Me	−41.25	>20	4.39 ± 1.04	>20	>20	>4.5

water molecules, allowing it to be displaced by potent inhibitors. This finding was crucial for accurate molecular modeling of the co-crystal structure, which showed inhibitor **1** displacing W1 in *Ca*BD2. Specifically, the conserved water W1 must be removed before performing ligand docking on *Ca*BD2 to achieve accurate binding predictions.

The experimental results obtained from the HTRF inhibition assays are generally consistent with the relative binding interaction energies predicted for our compound SAR suite **1a–1j** in the ligand docking analysis. A key role in binding is played by formation of a hydrogen bond between the hydrogen of the OH of the ligand and the W2 oxygen (Figure 2). The relatively lower activity of compounds **1a**, **1b**, and **1** may be due to the decreased pK_a of the phenol OH caused by introduction of the F substituent (7.86, 8.10, and 9.27 for **1a**, **1b** and **1**, respectively; calculated by MarvinSketch 20.3) (Figure S43).

Addition of a hydroxyl group ortho to the methyl group in position R3 in **1c** resulted in increased potency compared to substitution at the meta position (**1d**). This could be due to an increased distance from Leu420, weakening or preventing hydrogen bonding. Lowering the pK_a by replacing the methyl group with halogen atoms (—Cl, —Br, —I; compounds **1e–1g**) enhanced the potency up to 3-fold (Table 1 and Figure S42). The docking results predicted a slight difference in activities between these compounds (I > Br > Cl in order of decreasing potency), which was too small to detect in the experimental inhibition assays. The deprotonated forms of these compounds are predicted to form a hydrogen bond with the W5 water bridge. A pK_a calculation indicates that the —OH in all these halo-substituted ligands is deprotonated at pH 7, rationalizing the similar potencies observed. Whereas the potencies of compounds **1i** and **1j**, in which the methyl group on the phenyl ring was replaced by a nitro- or bromo- substituent, were similar to that of the original imidazopyridine **1**, an amino group at this position in compound **1h** yielded a 10-fold enhancement of potency, likely due to hydrogen bonding to Leu420 as predicted in the docking calculations.

5 | CONCLUSIONS

The discovery of inhibitor **1** demonstrated the feasibility of selectively inhibiting *Ca*BD2 vs human BET BD2.[17] The present study demonstrates the use and advantages of MD studies to facilitate the design of more potent and selective inhibitors. MD simulations provide a more realistic understanding of the binding mode and were here explored as a potential computational tool for design of drugs targeting fungal BDs. The co-crystal structure of **1** bound to *Ca*BD2 reveals that W1, a conserved water molecule close to the binding site, is missing when the bound ligand is present. Displacement of this water molecule by **1** is predicted by the MD analysis, in terms of lowered occupancy compared to the other conserved waters. This insight informed creation of a series of compounds predicted to have higher BD2 binding affinity than **1**.

Compounds chosen to have decreased pK_a (**1e–1g**) relative to **1** showed a 3- to 5-fold decrease in IC_{50} while still retaining good selectivity against human Brd4 BD2 (>10 fold). This confirms a role of the imidazole nitrogen in binding. The methyl group on the imidazopyridine ring also was found to contribute to selectivity. Compounds **1c** and **1h**, designed to form additional hydrogen bonds with Leu420 (Figure 6), showed a 5-fold (**1c**) or 10-fold (**1h**) decrease in IC_{50}. In conclusion, we identified and rationalized displacement of a structural water of *Ca*BD2, W1, using MD as a key mechanism in selective ligand binding to this site. This allowed development of a more accurate model for docking calculations and in silico SAR predictions, which were validated by experimental IC_{50} data. Apart from application to *Ca*BD2 as in the present study, this approach could be usefully extended to similar ligand-receptor systems to achieve more active compound predictions.

ACKNOWLEDGMENTS

Justin M. Overhulse was an NIH Chemical Biology Interface Predoctoral Trainee (T32 GM118289). Kaiyao Wei was supported by a CEA PhD fellowship. Charles E. McKenna thanks NIH (R21

1096987x, 2022, 32, Downloaded from https://onlinelibrary.wiley.com/doi/10.1002/jcc.26997 by Cea Grenoble, Wiley Online Library on [24/07/2024]. See the Terms and Conditions (https://onlinelibrary.wiley.com/terms-and-conditions) on Wiley Online Library for rules of use; OA articles are governed by the applicable Creative Commons License

AI113704) and the USC Bridge Institute for financial support. Carlo Petosa and Jérôme Govin acknowledge funding from the ANR (ANR-18-CE18-0007) and the Finovi Foundation. We thank Ms. Inah Kang for her invaluable assistance in the preparation of this manuscript.

DATA AVAILABILITY STATEMENT

The data that support the findings of this study are available from the corresponding author upon reasonable request.

ORCID

Jérôme Govin https://orcid.org/0000-0001-5511-6965
Carlo Petosa https://orcid.org/0000-0002-9975-1167
Charles E. McKenna https://orcid.org/0000-0002-3540-6663

REFERENCES

[1] B. J. Kullberg, M. C. Arendrup, *N. Engl. J. Med.* **2015**, *373*(15), 1445.
[2] F. Bongomin, S. Gago, R. O. Oladele, D. W. Denning, *J. Fungi* **2017**, *3*, 4.
[3] B. Halford, *Chem. Eng. News* **2021**, *99*, 7.
[4] H. H. Kong, J. A. Segre, *Science* **2020**, *368*(6489), 365.
[5] R. Rajendran, L. Sherry, C. J. Nile, A. Sherriff, E. M. Johnson, M. F. Hanson, C. Williams, C. A. Munro, B. J. Jones, G. Ramage, *Clin. Microbiol. Infect.* **2016**, *22*(1), 87.
[6] D. R. Giacobbe, A. E. Maraolo, V. Simeon, F. Magne, M. C. Pace, I. Gentile, P. Chiodini, C. Viscoli, M. Sanguinetti, M. Mikulska, M. Fiore, M. Bassetti, *Mycoses* **2020**, *63*(4), 334.
[7] Centers for Disease Control and Prevention. *Candida auris*. https://www.cdc.gov/fungal/candida-auris/index.html. Accessed 2021.
[8] J. A. Maertens, *Clin. Microbiol. Infect.* **2004**, *10*(Suppl 1), 1.
[9] M. W. Pound, M. L. Townsend, V. Dimondi, D. Wilson, R. H. Drew, *Med. Mycol.* **2011**, *49*(6), 561.
[10] D. Maubon, C. Garnaud, T. Calandra, D. Sanglard, M. Cornet, *Intensive Care Med.* **2014**, *40*(9), 1241.
[11] M. Masia Canuto, F. Gutierrez Rodero, *Lancet Infect. Dis.* **2002**, *2*(9), 550.
[12] M. C. Fisher, N. J. Hawkins, D. Sanglard, S. J. Gurr, *Science* **2018**, *360*(6390), 739.
[13] *Editorial. Nat. Microbiol.* **2017**, *2*(8), 17120.
[14] A. G. Cochran, A. R. Conery, R. J. Sims, 3rd., *Nat. Rev. Drug Discov.* **2019**, *18*(8), 609.
[15] E. Ferri, C. Petosa, C. E. McKenna, *Biochem. Pharmacol.* **2016**, *106*, 1.
[16] F. Mietton, E. Ferri, M. Champleboux, N. Zala, D. Maubon, Y. Zhou, M. Harbut, D. Spittler, C. Garnaud, M. Courcon, M. Chauvel, C. d'Enfert, B. A. Kashemirov, M. Hull, M. Cornet, C. E. McKenna, J. Govin, C. Petosa, *Nat. Commun.* **2017**, *8*, 15482.
[17] C. Y. Wang, P. Filippakopoulos, *Trends Biochem. Sci.* **2015**, *40*(8), 468.
[18] S. Kalyaanamoorthy, Y. P. Chen, *Drug Discov. Today* **2011**, *16*(17–18), 831.
[19] S. J. Macalino, V. Gosu, S. Hong, S. Choi, *Arch. Pharm. Res.* **2015**, *38*(9), 1686.
[20] M. I. Walton, P. D. Eve, A. Hayes, M. R. Valenti, A. K. De Haven Brandon, G. Box, A. Hallsworth, E. L. Smith, K. J. Boxall, M. Lainchbury, T. P. Matthews, Y. Jamin, S. P. Robinson, G. W. Aherne, J. C. Reader, L. Chesler, F. I. Raynaud, S. A. Eccles, I. Collins, M. D. Garrett, *Clin. Cancer Res.* **2012**, *18*(20), 5650.
[21] W. Yu, A. D. MacKerell, Jr., *Methods Mol. Biol.* **2017**, *1520*, 85.
[22] A. Acharya, R. Agarwal, M. B. Baker, J. Baudry, D. Bhowmik, S. Boehm, K. G. Byler, L. Coates, S. Y. Chen, C. J. Cooper, O. Demerdash, I. Daidone, J. D. Eblen, S. Ellingson, S. Forli, J. Glaser, J. C. Gumbart, J. Gunnels, O. Hernandez, S. Irle, J. Larkin, T. J. Lawrence, S. LeGrand, S. H. Liu, J. C. Mitchell, G. Park, J. M. Parks, A. Pavlova, L. Petridis, D. Poole, L. Pouchard, A. Ramanathan, D. Rogers, D. Santos-Martins, A. Scheinberg, A. Sedova, S. Shen, J. C. Smith, M. D. Smith, C. Soto, A. Tsaris, M. Thavappiragasam, A. F. Tillack, J. V. Vermaas, V. Q. Vuong, J. Yin, S. Yoo, M. Zahran, L. Zanetti-Polzi, *J. Chem. Inform. Model.* **2020**, *60*(12), 5832.
[23] Oak Ridge National Laboratory, Oak ridge national laboratory ORNL launches summit supercomputer. https://www.ornl.gov/news/ornl-launches-summit-supercomputer. Accessed **2021**.
[24] A. A. Sadybekov, A. V. Sadybekov, Y. Liu, C. Iliopoulos-Tsoutsouvas, X. P. Huang, J. Pickett, B. Houser, N. Patel, N. K. Tran, F. Tong, N. Zvonok, M. K. Jain, O. Savych, D. S. Radchenko, S. P. Nikas, N. A. Petasis, Y. S. Moroz, B. L. Roth, A. Makriyannis, V. Katritch, *Nature* **2022**, *601*(7893), 452.
[25] K. Roos, C. Wu, W. Damm, M. Reboul, J. M. Stevenson, C. Lu, M. K. Dahlgren, S. Mondal, W. Chen, L. Wang, R. Abel, R. A. Friesner, E. D. Harder, *J. Chem. Theory Comput.* **2019**, *15*(3), 1863.
[26] T. A. Halgren, *J. Chem. Inf. Model.* **2009**, *49*(2), 377.
[27] J. Huang, S. Rauscher, G. Nawrocki, T. Ran, M. Feig, B. L. de Groot, H. Grubmuller, A. D. MacKerell Jr., *Nat. Methods* **2017**, *14*(1), 71.
[28] M. Seeber, M. Cecchini, F. Rao, G. Settanni, A. Caflisch, *Bioinformatics* **2007**, *23*(19), 2625.
[29] M. Seeber, A. Felline, F. Raimondi, S. Muff, R. Friedman, F. Rao, A. Caflisch, F. Fanelli, *J. Comput. Chem.* **2011**, *32*(6), 1183.
[30] L. R. Vidler, N. Brown, S. Knapp, S. Hoelder, *J. Med. Chem.* **2012**, *55*(17), 7346.
[31] P. G. Clark, L. C. Vieira, C. Tallant, O. Fedorov, D. C. Singleton, C. M. Rogers, O. P. Monteiro, J. M. Bennett, R. Baronio, S. Muller, D. L. Daniels, J. Mendez, S. Knapp, P. E. Brennan, D. J. Dixon, *Angew. Chem. Int. Ed. Engl.* **2015**, *54*(21), 6217.
[32] F. M. Ferguson, O. Fedorov, A. Chaikuad, M. Philpott, J. R. Muniz, I. Felletar, F. von Delft, T. Heightman, S. Knapp, C. Abell, A. Ciulli, *J. Med. Chem.* **2013**, *56*(24), 10183.
[33] D. Huang, E. Rossini, S. Steiner, A. Caflisch, *ChemMedChem* **2014**, *9*(3), 573.

SUPPORTING INFORMATION

Additional supporting information can be found online in the Supporting Information section at the end of this article.

How to cite this article: Y. Zhou, J. M. Overhulse, N. J. Dupper, Y. Guo, B. A. Kashemirov, K. Wei, J. Govin, C. Petosa, C. E. McKenna, *J. Comput. Chem.* **2022**, *43*(32), 2121. https://doi.org/10.1002/jcc.26997

1096987x, 2022, 32, Downloaded from https://onlinelibrary.wiley.com/doi/10.1002/jcc.26997 by Cea Grenoble, Wiley Online Library on [24/07/2024]. See the Terms and Conditions (https://onlinelibrary.wiley.com/terms-and-conditions) on Wiley Online Library for rules of use; OA articles are governed by the applicable Creative Commons License